ADVANCED FUNCTIONAL MATERIALS
www.afm-journal.de

Doping Strategies for Tetrasubstituted Paracyclophane Hole Transport Layers in Perovskite Solar Cells

*Alexander Deniz Schulz, Steffen Andreas Otterbach, Henrik Tappert, David Elsing, Wolfgang Wenzel, Mariana Kozlowska, Stefan Bräse, Alexander Colsmann, and Holger Röhm**

Because of its excellent hole conductivity, p-doped 2,2′7,7′-tetrakis-(*N*,*N*-di-p-methoxyphenyl-amine)-9,9′-spiro-bifluorene (spiro-MeOTAD) is commonly deployed for hole transport in organic metal halide perovskite solar cells, but its rather expensive synthesis prompts the research for alternatives. In this work, tetrasubstituted [2.2]paracyclophanes (PCPs) are synthesized and investigated for replacing spiro-MeOTAD. To enhance their conductivity, different doping strategies are followed. Best conductivities are achieved by doping PCP thin films with tris(2-(1*H*-pyrazol-1-yl)-4-*tert*-butylpyridine) cobalt(III) tris(bis(trifluoromethylsulfonyl)imide) (FK209), matching the conductivity of state-of-the-art p-doped spiro-MeOTAD. Best performance in solar cells is leveraged by doping PCPs with the co-dopants lithium bis(trifluoromethanesulfonyl)imide (LiTFSI) and 4-*tert*-butylpyridine (tBP) which are also used to p-dope spiro-MeOTAD thin films in solar cells. Yet, the thermal device stability is maximized upon doping PCPs with FK209 and 2,3,5,6-tetrafluoro-7,7,8,8-tetracyanoquinodimethane (F_4TCNQ).

1. Introduction

In perovskite solar cells (PSCs) with regular device architecture, hole collection at the electrodes is most often facilitated by hole transport layers of spiro-MeOTAD.[1] Spiro-MeOTAD can be readily processed into homogeneous thin films, it exhibits good hole conductivity when electrically doped, and has been instrumental in the evolution of PSCs.[2] The search for cost-effective alternatives has given rise to the investigation of PCPs, a material class for hole transport that leverages comparable power conversion efficiencies in PSCs.[3–6] Substitutions at donor groups in these molecules offer a wide range of adaptability in terms of solubility and ionization potential (IP).[6]

In order to achieve appropriate conductivity, spiro-MeOTAD is commonly doped with LiTFSI:tBP. Upon exposure to oxygen, spiro-MeOTAD forms weakly bound donor-acceptor complexes, i.e., spiro-MeOTAD$^+O_2^-$, due to the low IP of spiro-MeOTAD and the high electron affinity (EA) of molecular oxygen. The O_2^- anion is then exchanged with the $TFSI^-$ anion from Li^+TFSI^- to form spiro-MeOTAD$^+TFSI^-$ and lithium oxide.[7] It was reported that water can also be involved in the oxidation process.[8,9] The positive charge on spiro-MeOTAD$^+$ is only weakly bound to the delocalized negative charge on the $TFSI^-$ anion, hence constituting a mobile hole.[7,10] tBP is not part of the redox reaction, but it increases the solubility of LiTFSI in chlorobenzene (CB) and significantly influences the layer morphology of LiTFSI-doped spiro-MeOTAD

A. D. Schulz, S. Bräse, A. Colsmann, H. Röhm
Material Research Center for Energy Systems (MZE)
Karlsruhe Institute of Technology (KIT)
Kaiserstrasse 12, 76131 Karlsruhe, Germany
E-mail: holger.roehm@kit.edu
A. D. Schulz, A. Colsmann, H. Röhm
Light Technology Institute (LTI)
Karlsruhe Institute of Technology (KIT)
Kaiserstrasse 12, 76131 Karlsruhe, Germany
S. A. Otterbach, H. Tappert, S. Bräse
Institute of Organic Chemistry (IOC)
Karlsruhe Institute of Technology (KIT)
Kaiserstrasse 12, 76131 Karlsruhe, Germany
D. Elsing, W. Wenzel, M. Kozlowska
Institute of Nanotechnology (INT)
Karlsruhe Institute of Technology (KIT)
Kaiserstrasse 12, 76131 Karlsruhe, Germany
S. Bräse
Institute of Biological and Chemical Systems – Functional Molecular Systems (IBCS-FMS)
Karlsruhe Institute of Technology (KIT)
Kaiserstrasse 12, 76131 Karlsruhe, Germany
The ORCID identification number(s) for the author(s) of this article can be found under https://doi.org/10.1002/adfm.202402110

DOI: 10.1002/adfm.202402110

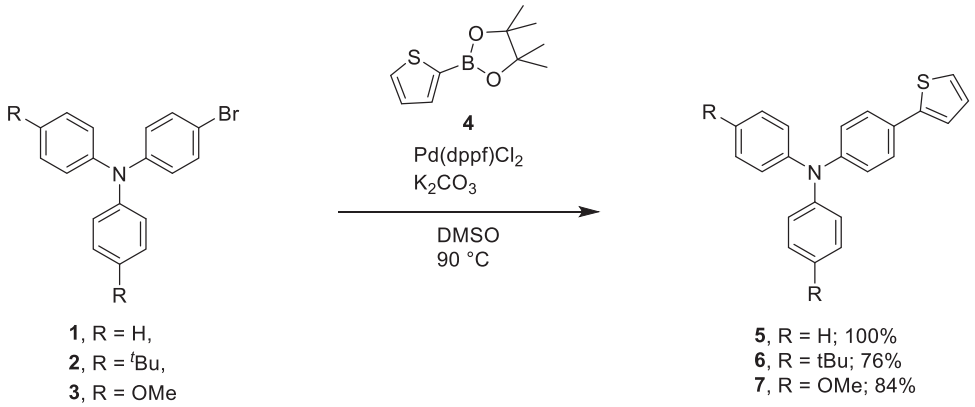

Figure 1. Synthetic procedure for Suzuki coupling of the TPA donor units (**1**, **2**, **3**) and the thiophene π-bridge.

thin films.[11] Furthermore, tBP is known to decrease recombination at surface defects, resulting in enhanced open-circuit voltages of solar cells.[12] While frequently deployed for doping of spiro-MeOTAD and novel hole transport layers (HTLs),[13–16] both LiTFSI and tBP are detrimental to the device stability: tBP is corrosive to the perovskite due to dissolution of and complex formation with PbI_2.[17–19] Furthermore, it evaporates over time, leaving behind pinholes and aggregated LiTFSI. The hygroscopicity of LiTFSI promotes the degradation of the perovskite in case of water ingress.[11] Although innovative approaches have been reported to mitigate these effects, such as binding tBP in a complex by halogen bonding or replacing tBP with pyridine moieties in the hole transport material's (HTM) structure,[19,20] avoiding the use of LiTFSI is desirable.

Over the last few years, FK209 has become increasingly popular as a third doping component in addition to LiTFSI:tBP.[13,14,16] Yet, FK209 can also oxidize spiro-MeOTAD on its own and without any exposure to oxygen. In this process, Co(III) is reduced to Co(II) and one of the TFSI ions becomes the counterion to spiro-MeOTAD$^+$.[21] Another common dopant for organic semiconductors, which has been used for spiro-MeOTAD, is F_4TCNQ.[22,23] F_4TCNQ forms a ground state charge transfer complex with spiro-MeOTAD. Both FK209 and F_4TCNQ are commercially available at moderate cost. This prompted us to explore p-doping of PCPs by FK209 and F_4TCNQ and to compare the results to doping with LiTFSI:tBP, which was used in previous reports of PCPs.[3–5]

We synthesize novel tetrasubstituted PCPs and systematically investigate their optoelectronic properties, particularly their charge carrier dynamics and p-doping. Quantum mechanical calculations demonstrate the electronic structure of these molecules and identify the optical transitions of oxidized tetrasubstituted PCPs (i.e., their cations), which aids the interpretation of UV-Vis-NIR spectra. We employ metal-insulator-semiconductor charge extraction by linearly increasing voltage (MIS-CELIV) in order to investigate the charge carrier dynamics of neat and doped PCPs. Finally, we implement p-doped PCP layers into solar cells and test the performance and thermal stability of devices in dependence of the HTL's doping.

2. Results and Discussion

2.1. Synthesis of Thiophene-Bridged Tetrasubstituted PCPs

PCP was previously substituted with triphenylamine (TPA) donor groups either directly or with ethene π-bridges in between. Recently, we demonstrated cost-efficient disubstituted PCPs with thiophene π-bridges. Substitution of TPA in *para*-position with methoxy or *tert*-butyl groups allowed for tuning of the IP via mesomeric and inductive donor effects, respectively.[6] Both groups increased the solubility of molecules by preventing their aggregation and promoting interactions with organic solvents.

Here, we synthesized three different tetrasubstituted PCPs with TPA donor groups attached via thiophene π-bridges and additional substitution of TPA in *para*-position. In the first target compound (**TPCP-1**), unsubstituted TPA was used, while the second (**TPCP-2**) and third (**TPCP-3**) target compounds feature methoxy- and *tert*-butyl-substitutions in the *para*-positions of the TPA units.

The tetrasubstituted PCPs were synthesized as depicted in **Figure 1** using consecutive cross-couplings. In a first step, the desired donor moiety was attached to thiophene via Suzuki coupling. For this, the TPAs **1**, **2**, and **3** and 2-pinacolborylthiophene (**4**) were prepared following literature procedures.[24–26] These were coupled using a common Suzuki cross-coupling setup with $Pd(dppf)Cl_2$ and K_2CO_3 in dimethyl sulfoxide (DMSO) at 90 °C, resulting in yields of 100%, 76%, and 84% for **5**, **6**, and **7**, respectively.

The subsequent quadruple coupling of **5**, **6**, and **7** to the PCP core could not be achieved in sufficient yields via Suzuki coupling or by CH activation, which worked well for disubstituted PCPs.[6] Therefore, we followed the strategy published by Kobayakawa et al.,[27] who used Negishi cross-coupling to connect two thiophene moieties with a pseudo-*ortho* iodinated [2.2]paracyclophane. To obtain the required Negishi reactant, Kobayakawa et al. lithiated thiophene with *n*-butyllithium and then added a zinc chloride solution. With the Negishi reactant ready, the [2.2]paracyclophane was introduced to the reaction. Eventually, they isolated the desired disubstituted product with a yield of 85%. We slightly modified this protocol regarding temperature and catalyst, i.e., PEPPSI-IPr was used to optimize the

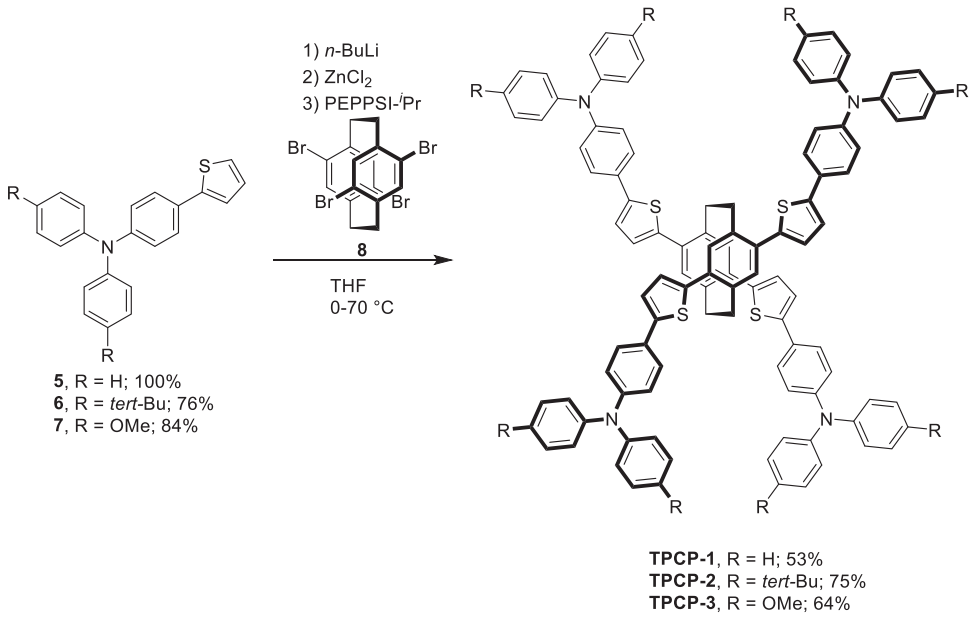

Figure 2. Synthetic procedure for Negishi coupling of the thiophene substituted donor units (5, 6, 7) with tetrabromo-PCP to obtain the target compounds.

yield for the fourfold coupling of units **5**, **6**, and **7** with tetrabromo[2.2]paracyclophane (**8**) as depicted in **Figure 2**. This optimized step yielded 53%, 75% and 64% of **TPCP-1**, **TPCP-2**, and **TPCP-3**, respectively. Hence, the methoxy and *tert*-butyl substituents raised the yield of the final product by 11 or 22% absolute, respectively.

All three final products exhibited solubilities of more than 30 g L^{-1} in CB, which was beneficial for device processing. Yet, the unsubstituted **TPCP-1** showed aggregation during storage, while the *tert*-butyl- and methoxy-substituted **TPCP-2** and **TPCP-3** remained fully dissolved in CB over several months. All three TPCPs exhibited good thermal stability with glass transition temperatures above 140 °C (Figure S1, Supporting Information).

In order to assess the economic feasibility of **TPCP**s as an alternative to spiro-MeOTAD, we carried out a cost estimate of **TPCP-3**. This estimate shows that even without further optimization of the synthesis, **TPCP-3** can be produced at 25% of the cost of spiro-MeOTAD (Table S1, Supporting Information).

2.2. Optoelectronic Properties

An ideal HTL both facilitates hole transport without ohmic losses and blocks electrons from diffusing into the anode in order to prevent electrode recombination losses. Hence, HTLs are generally designed for a high hole conductivity, an IP that matches the perovskite's IP and a wider energy gap than the band gap of the perovskite. A wide optical gap (E_g^{opt}) of the HTL also prevents parasitic light absorption.

We determined E_g^{opt} of **TPCP** solutions in CB by analyzing the Tauc plots of UV-vis absorbance spectra, depicted in **Figure 3a**. By applying linear fits around the inflection points, we obtained E_g^{opt} between 2.43 and 2.50 eV for all three **TPCP**s. This was ≈400 to 500 meV narrower than E_g^{opt} of the reference spiro-MeOTAD, i.e., 2.93 eV. We confirmed E_g^{opt} by studying the transitions from the ground state of the molecule, S_0, and the lowest singlet excited state S_1 by time-dependent density functional theory (TD-DFT) calculations. **Table 1** summarizes the results which also agree with the experimental findings within negligible deviations of up to 0.06 eV with a slight dependence on the size of the localized basis set. Visualizations of the transition orbitals involved in the excitations and the orbital energies are provided in Figures S2–S4 and Tables S2–S7 (Supporting Information).

Thus, **TPCP**s exhibit some parasitic photon absorption in the blue spectral regime. However, the strong absorption of the perovskite in the blue diminishes any parasitic absorption of blue photons in the HTL on the back side of the device.[28]

To assess the matching of the transport energies of the HTLs and the perovskite layer, we experimentally determined the IPs by photoelectron spectroscopy in air (PESA).[29–31] Figure 3b depicts representative PESA measurements on **TPCP-1**, **TPCP-2**, and **TPCP-3** thin films. Fitting the photoelectron yield versus the photon energy for three samples each, we found IPs of 5.42, 5.34, and 5.27 eV, respectively, which were larger than the IP of spiro-MeOTAD at 5.12 eV. The mesomeric donor effect of the methoxy group in **TPCP-3** was noticeable with a lowering of the IP by 150 meV against the unsubstituted **TPCP-1**. The inductive donor effect of the *tert*-butyl group in **TPCP-2** also reduced the IP, but the impact was smaller.

We also measured IPs of the **TPCP**s in solution with cyclic voltammetry (CV) (Table 1; and Figure S5 and Table S8, Supporting Information). We observed the same IP trend as in PESA measurements and DFT calculations, but owing to the polar solvent environment and different states of aggregation compared to a solid thin film,[32,33] the IPs obtained from CV were smaller by ≈200 meV. For comparison, the IP of the perovskite methylammonium lead iodide ($MAPbI_3$) is reported at ≈5.6 eV.[34,35]

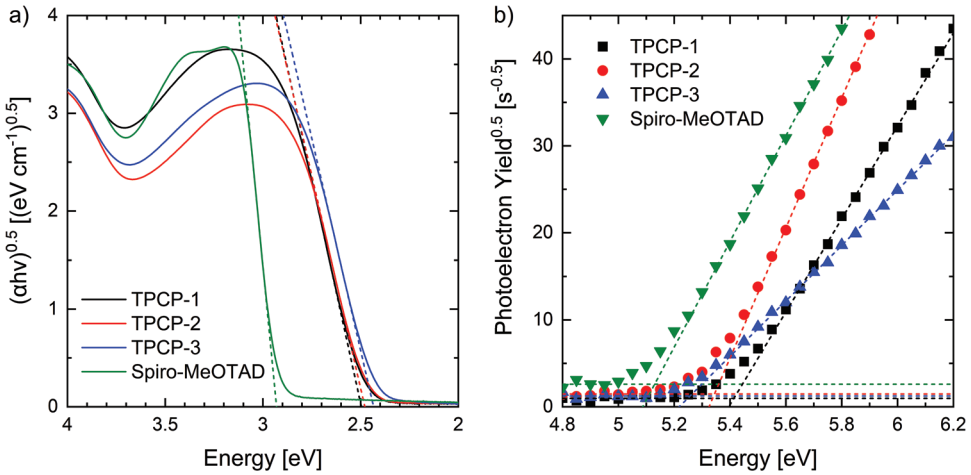

Figure 3. a) Tauc plots of the UV–vis absorbance spectra of the **TPCP** compounds in CB (30 µg mL^{-1}). b) According to PESA measurements, the IPs range between 5.27 and 5.42 eV also matching the requirements of application in PSCs. Lower slopes in PESA measurements indicate lower photoelectron emission rate, e.g., due to the permeability and thickness of the layer, which are largely independent from the IP.

We also calculated the IPs of all three TPCPs via density functional theory (DFT) in vacuo (for the lowest energy conformer), resulting in 5.58, 5.43, or 5.26 eV, respectively. The slight differences in the calculated and the experimentally measured IPs likely stem from the treatment as an isolated molecule in the simulation while PESA is measured on solid-state thin films. However, DFT calculations and PESA measurements show the same trend of IPs between all three **TPCP**s as shown in Table 1.

Hence, the IPs of all investigated **TPCP** compounds are suitable to be used as HTLs in $MAPbI_3$ solar cells. Due to their slightly larger IPs compared to spiro-MeOTAD, they may also be applied to wide-bandgap perovskites that typically have larger IPs than $MAPbI_3$.[36,37]

2.3. Hole Mobilities in TPCP Thin Films

HTLs must have a certain minimal thickness to ensure complete coverage of the underlying layer in a thin-film device in order to mitigate imperfections from the fabrication process. For the purpose of minimizing ohmic losses and avoiding space-charge limitation of the hole current, the HTL should possess a high hole conductivity $\sigma = q \bullet p \bullet \mu_h$, which is proportional to the hole density p, the hole mobility μ_h, and the elementary charge q. In order to determine the hole mobilities of the **TPCP**s, we employed MIS-CELIV.[40,41] Holes were injected through a molybdenum oxide (MoO_x)/silver electrode into the **TPCP** thin films, where they accumulated at the opposite interface to an insulating lithium fluoride layer (LiF, 20 nm). Then, a linear voltage ramp was applied to extract the previously injected holes from the **TPCP** thin film. The charge carrier reservoir mimics an ohmic contact, creating a space-charge limited transient current, which is overlaid with the displacement current J_0 of the geometric capacitance. The time at which twice the displacement current is reached, i.e., t_{2J0}, is related to µ as reported by Sandberg et al.[41] **Figure 4** shows the transient curves obtained for **TPCP-1**, **TPCP-2**, **TPCP-3**, and spiro-MeOTAD thin films. J_0 was determined using an injection voltage of −3 V. We found that this negative injection voltage was necessary to deplete spiro-MeOTAD of holes from unintentional doping and to obtain an accurate J_0. No unintentional doping was found in the **TPCP**s. A comparison of hole extraction at injection voltages of 0 and −3 V and further discussion of unintentional doping can be found in the supporting information (Figure S6, Supporting Information).[8,42] Notably, J_0 contains information about the quasi-static relative permittivity (ϵ_s) of the semiconductor layer which influences the electric field distribution in the solar cell. By treating the insulator and the semiconductor layers as two parallel plate capacitors connected in series, we obtained $\epsilon_s = 3.2 \pm 0.1$ for the unsubstituted **TPCP-1**. The *tert*-butyl-substituted **TPCP-2** exhibited a lower permittivity of $\epsilon_s = 2.7 \pm 0.2$, while the methoxy-substituted **TPCP-3** had a higher permittivity of $\epsilon_s = 4.1 \pm 0.2$,

Table 1. Summary of the optical and electronic properties of the **TPCP** compounds obtained from UV-vis spectroscopy, PESA, CV, and DFT calculations. Data of spiro-MeOTAD are provided for reference.

Compound	E_g^{opt} [eV]	$E_g^{opt, TD\text{-}DFT}$ [eV]	E_{IP}^{PESA} [eV]	E_{ox}^{CV} [V]	E_{IP}^{CV} [a] [eV]	E_{IP}^{DFT} [eV]
TPCP-1	2.50	2.50 (2.56[b])	5.42 ± 0.01	0.39	5.19	5.58 (5.46–5.62)[c]
TPCP-2	2.48	2.46(2.53[b])	5.34 ± 0.01	0.25	5.15	5.43 (5.31–5.43)[c]
TPCP-3	2.43	2.38 (2.43[b])	5.27 ± 0.04	0.36	5.06	5.26 (5.13–5.27)[c]
Spiro-MeOTAD	2.93	3.11[38]	5.12 ± 0.03	–	–	–

[a] Potential ferrocene (Fc) ($E^\circ(Fc^+/Fc) = 0.400$ V vs NHE).[39] [b] Calculated with the def2-SVP basis set. [c] Range for different conformers (see Supporting Information).

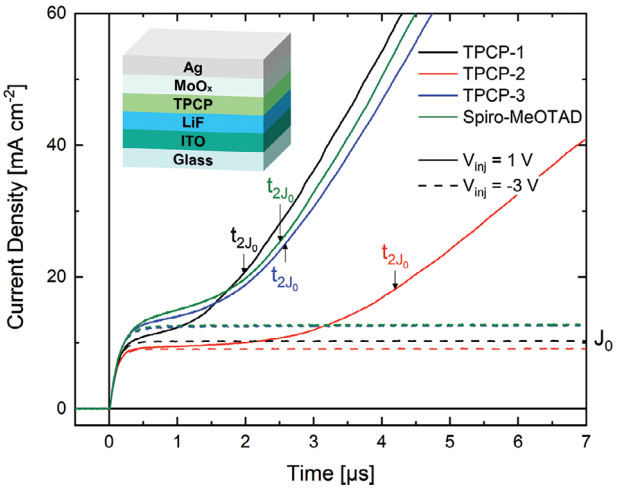

Figure 4. MIS-CELIV characteristics of thin films of neat **TPCP**s and spiro-MeOTAD. The relative permittivity ϵ_s of each compound was calculated from the respective displacement current J_0. After injection through the MoO_x/Ag top electrode by a constant injection voltage (V_{inj}), holes form a reservoir of charge carriers at the interface to the LiF layer. Subsequently, this charge carrier reservoir mimics an ohmic contact, producing a space-charge limited current upon extraction via a linear voltage ramp (400 mV µs^{-1}) starting at $t = 0$. The slope of the transient current is related to the hole mobility μ_h, which is largest for **TPCP-1**.

which was very similar to the permittivity of spiro-MeOTAD ($\epsilon_s = 4.0 \pm 0.2$).

At an injection voltage of 1 V, the slope of the transient current saturated in all compounds (Figure S7, Supporting Information), allowing for consistent measurements of t_{2J0} and, hence, the calculation of μ_h.[41] **TPCP-1** achieved an excellent $\mu_h = (3.7 \pm 0.3) \cdot 10^{-5}$ cm^2·V^{-1} s^{-1}, outperforming both the spiro-MeOTAD reference and **TPCP-3** (both $\mu_h = (2.7 \pm 0.3) \cdot 10^{-5}$ cm^2 V^{-1} s^{-1}). **TPCP-2** had a lower $\mu_h = (1.1 \pm 0.1) \cdot 10^{-5}$ cm^2 V^{-1} s^{-1}, which may be explained by its bulky *tert*-butyl units that are not part of the molecule's π-electron system and hence do not contribute to charge carrier delocalization (see visualization of the HOMO in Figure S3, Supporting Information). Overall, the hole mobilities are promising but still insufficient for use as neat HTLs in high-performance PSCs. To achieve good hole conductivity, the hole mobility or the hole density have to be increased.

2.4. Electrical Doping of TPCP

Charge carrier densities and thus conductivities in semiconductors are commonly increased by electrical doping. Organic semiconductors can be p-doped by introducing strong electron acceptors, which oxidize the organic semiconductor, creating radical cations.

2.4.1. Energetics of Doping

To assess p-doping of **TPCP**s, we examined the acceptor strength of suitable dopants (i.e., the EA) and the IPs of the HTLs. The EA of F_4TCNQ was reported between 5.08 and 5.24 eV, measured by inverse photoelectron spectroscopy,[43,44] and 5.23 to 5.33 eV according to CV measurements.[45,46] However, its actual EA depends strongly on the host material.[47] FK209 was reported to have an EA of 5.12 eV, determined by differential pulse voltammetry.[21] In relation to the IPs of the **TPCP**s (i.e., between 5.27 and 5.42 eV), the EAs of F_4TCNQ and FK209 initially appear insufficient to foster charge transfer between dopants and **TPCP**s. However, the Coulomb binding energy of the ground state charge transfer complex and energetic disorder in organic semiconductors make the charge transfer energetically more favorable by several hundred meV.[48] Since the energy differences between the IPs of **TPCP**s and the EAs of F_4TCNQ and FK209 deviate only slightly, both dopants can still be efficient.

Upon doping of the HTMs and the formation of radical cations, a change in absorption is expected due to newly available electronic transitions from and into the singly occupied molecular orbital (SOMO) of the cation. These new transitions, which are characteristic of cationic species, appear red-shifted against the original features of the absorption spectrum. Therefore, a molecule that has an E_g^{opt} in the UV spectral regime in its undoped state may absorb visible or near-infrared light after oxidation. Such observations were reported for spiro-MeOTAD cations by Fantacci et al. and Cappel et al.[38,49] Our quantum mechanical calculations identify the transition orbitals involved in the excitation of **TPCP** cations (Tables S5–S7, Supporting Information). The respective calculated absorption spectra are illustrated in **Figure 5**. The emergence of new absorption bands is clearly visible from the comparison of spectra of neutral and cationic forms of **TPCP**s. The electron density difference for some characteristic transitions is depicted in the insets of Figure 5.

2.4.2. Doping in Solution

We conducted experimental doping of the **TPCP**s in CB by adding F_4TCNQ at a concentration of 10 wt.% or FK209 at a concentration of 50 wt.% (with respect to the mass of the HTM), which yielded comparable molar ratios (Table S9, Supporting Information). In order to produce strong doping signatures in optical measurements, we deliberately chose high dopant concentrations. Immediately after addition of the dopant, the color of all HTM solutions changed from completely transparent or light-yellow to black (Figure S8, Supporting Information). UV-Vis-NIR absorption measurements of diluted HTM solutions in CB demonstrate that this color change indeed originated from integer charge transfer (**Figure 6**; Figure S9, Supporting Information). Neutral F_4TCNQ and the HTMs absorb in the same spectral regime (close to 3 eV) which makes it difficult to differentiate between the two.[50] We observed increased absorbance in this regime for all HTM solutions containing F_4TCNQ, indicating the presence of F_4TCNQ in its neutral form. However, all of these solutions also exhibited characteristic absorption features of the F_4TCNQ^- anion in the visible (3.2 eV) and near-infrared (1.5 eV) spectral regime, indicating the formation of ground state charge-transfer complexes. These absorption features were much less pronounced in the doped **TPCP** solutions (Figure 6a–c) than in the doped spiro-MeOTAD reference (Figure 6d). This indicated that doping of spiro-MeOTAD with F_4TCNQ was much more efficient than doping of the TPCPs with F_4TCNQ. Accordingly, spiro-MeOTAD doped

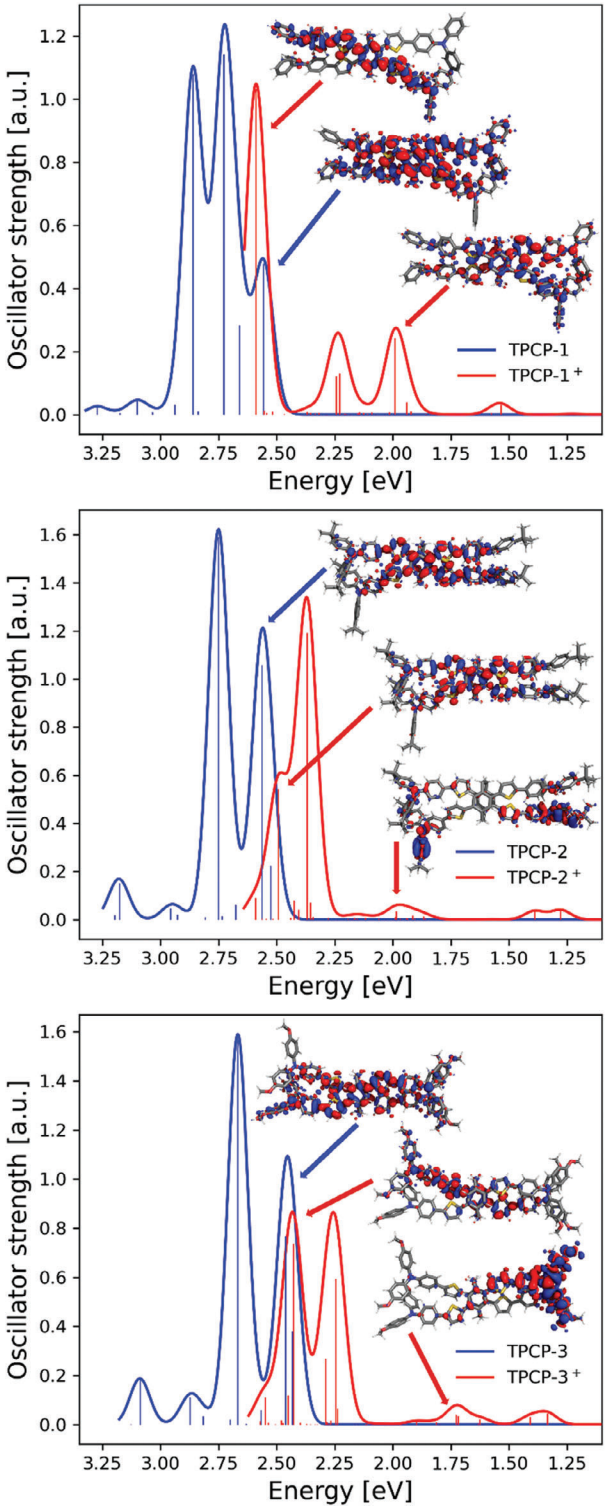

Figure 5. Calculated absorption spectra of the three TPCP molecules studied in their neutral and oxidized (p-doped) states using TD-B3LYP/def2-SVP level of theory in the gas phase. The electron density differences between the excited and the ground state of TPCPs, which in first place stem from some pronounced absorption bands, are depicted in visualizations of the molecules. Regions in red indicate a positive difference, i.e., electron accepting, while regions in blue indicate a negative difference, i.e., electron donating.

with F_4TCNQ also exhibited noticeable absorption features of the spiro-MeOTAD$^+$ cation in the visible and the near-infrared.[38,49]

Upon doping with FK209, distinct absorption bands of HTM cations appeared not only in spiro-MeOTAD, but also in the **TPCP**s. Specifically, new characteristic bands emerged between 2.1 and 1.5 eV as well as below 1.3 eV. Yet, in comparison to the calculated spectra (Figure 5), the absorption bands in the measured spectra (Figure 6) are red-shifted and show more broadening. In the experimental spectra of FK209-doped solutions, which contain both neutral molecules and their cations, the absorption features at ≈3 eV were less pronounced due to oxidation of the HTM molecules (Figure S9, Supporting Information). The strongest change in absorption upon addition of FK209 occurred in **TPCP-3** and spiro-MeOTAD, indicating more efficient doping compared to **TPCP-1** and **TPCP-2**. Remarkably, the main absorbance peak of **TPCP-3** (at 2.98 eV) was reduced by 16%, which was similar to the reduction in absorbance found in spiro-MeOTAD (at 3.18 eV), even though the IP of **TPCP-3** is 150 meV larger. This shows that FK209 is a significantly stronger dopant for **TPCP** than F_4TCNQ.

2.4.3. Enhancing the Conductivity of TPCP Thin Films via p-Doping

In order to quantify the doping efficiency as well as the impact of electrical doping on the conductivity in solid-state samples, we conducted measurements using the same MIS-CELIV device architecture as shown in Figure 4. MIS-CELIV theory assumes no background charge carriers to be present or only charge carriers that diffuse from the electrodes into the device.[40,41] Therefore, it cannot be readily applied to electrically doped samples. Instead, we performed two modified MIS-CELIV measurements, one in the doping-induced capacitive regime to obtain the doping concentration and one in the ohmic regime to obtain the conductivity.[51–53] We observed that the conductivity of **TPCP-3** and spiro-MeOTAD was improved by more than one order of magnitude upon doping, while the conductivity of **TPCP-1** and **TPCP-2** was improved only marginally. Furthermore, FK209-doped **TPCP-1** and **TPCP-2** solutions in chlorobenzene showed precipitation of material (Figure S10, Supporting Information), which we attribute to poor solubility of FK209 Co(III) TFSI in comparison to FK209 Co(II) TFSI. Therefore, in the following, we focus on the investigation of **TPCP-3** and benchmark its properties against spiro-MeOTAD.

F_4TCNQ-doped samples were too leaky for the determination of doping concentrations from capacitive measurements, but the conductivity could be determined from the ohmic regime. In contrast, on FK209-doped samples, both capacitive and ohmic measurements yielded useful insights. We excluded CELIV measurements on TPCP-3 or spiro-MeOTAD samples which were doped with LiTFSI:tBP since the slope of the transient current did not saturate with increasing injection voltages.

Figure 7 shows the conductivity of **TPCP-3** and spiro-MeOTAD thin films versus dopant concentration (FK209 or F_4TCNQ), derived from the ohmic regime MIS-CELIV measurements (Figures S11 and S12, Supporting Information). In neat films, the conductivity of spiro-MeOTAD was higher than the conductivity of **TPCP-3**, which we attribute to the already known unintentional doping of spiro-MeOTAD (Figure S6, Supporting

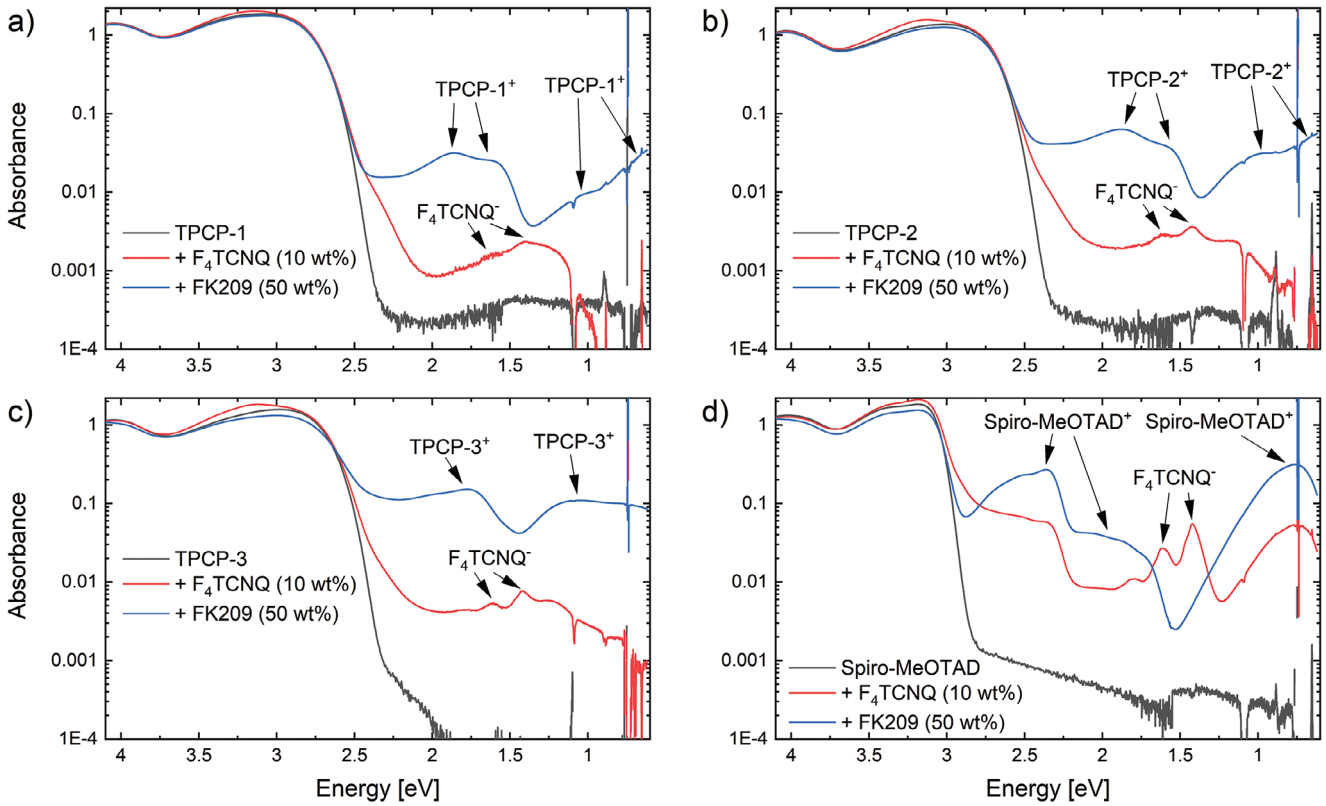

Figure 6. Absorbance spectra of doped (red and blue curves) and undoped (black curve) solutions of **TPCP-1**, **TPCP-2**, **TPCP-3,** and spiro-MeOTAD (30 µg mL^{-1} in CB), on logarithmic scale to better visualize the doping signatures. The addition of FK209 to the HTMs led to the emergence of absorption features of the HTM cations in the visible and near-infrared spectral regime, indicating doping. Upon addition of F_4TCNQ, weak absorption features of the F_4TCNQ^- anion appeared. At 0.74 eV, the strong absorption of CB produced minor measurement artifacts.

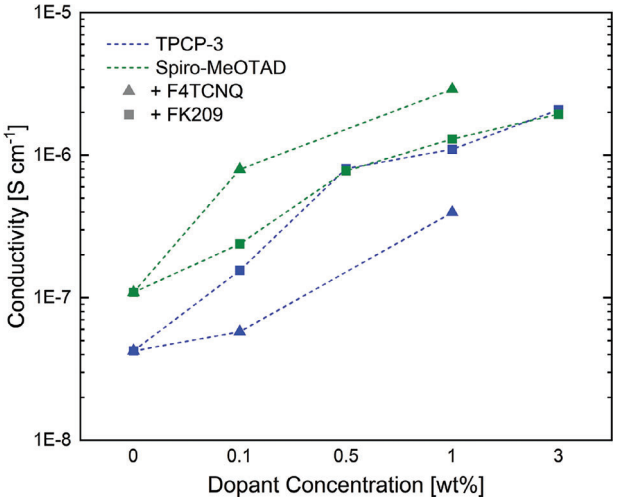

Figure 7. Conductivity of **TPCP-3** and spiro-MeOTAD thin films electrically doped with F_4TCNQ or FK209 versus dopant concentration. F_4TCNQ-doping was less efficient in increasing the conductivity in **TPCP-3** than in spiro-MeOTAD, but with FK209-doping the conductivities of **TPCP-3** and spiro-MeOTAD converged. We note that the data points are not evenly spaced along the x-axis and dashed lines between data points serve to guide the eye.

Information).[8,42] Taking into account the hole mobility and the conductivity from MIS-CELIV measurements in the standard and ohmic regimes, we calculated a hole density of $2.5 \cdot 10^{16}$ cm^{-3} from unintentional doping. Upon electrical doping with F_4TCNQ or FK209, the conductivity of spiro-MeOTAD increased with higher doping concentrations. F4TCNQ doping led to a greater increase in conductivity at the same concentration by weight. Notably, the molecular weight of FK209 is 5.4 times higher than the molecular weight of F_4TCNQ and hence the molar concentration of FK209 is only 18% of the molar concentration of F_4TCNQ at the same content by weight. Yet, FK209-doping increased the conductivity of **TPCP-3** more than F_4TCNQ-doping even at the same weight percentage (lower molar percentage). This suggests that the poor F_4TCNQ-doping efficiency in solution also translated to the thin film. Remarkably, **TPCP-3** doped with FK209 at a concentration of 3 wt.% achieved comparable conductivity to spiro-MeOTAD doped at the same concentration.

The primary goal of doping is the enhancement of the conductivity of the semiconductor by increasing the free charge carrier density. Yet, doping can also affect the conductivity by changing the charge carrier mobility. This change is related to the dependence of the charge carrier mobility on the charge carrier density as well as Coulomb forces between the generated charge carriers on the organic semiconductor and the counter-charges on the dopants.[54–56] The former leads to increased mobility at

Table 2. Charge carrier density (N_p), doping efficiency (η), conductivity (σ), and hole mobility (μ_h) of **TPCP-3** and spiro-MeOTAD thin films doped with FK209. The data was derived from ohmic and capacitive regime MIS-CELIV measurements.

Sample	N_p [10^{18} cm^{-3}]	Doping η [%]	σ [10^{-6} S cm^{-1}]	μ_h [10^{-6} cm^2 V^{-1} s^{-1}]
TPCP-3 + FK209 (0.5 wt%)	1.76 ± 0.08	67 ± 6	0.81 ± 0.04	2.8 ± 0.3
TPCP-3 + FK209 (1 wt%)	3.46 ± 0.16	66 ± 6	1.10 ± 0.05	1.9 ± 0.2
Spiro-MeOTAD + FK209 (0.5 wt%)	1.56 ± 0.08	62 ± 5	0.78 ± 0.04	3.0 ± 0.3
Spiro-MeOTAD + FK209 (1 wt%)	3.00 ± 0.14	60 ± 5	1.30 ± 0.06	2.6 ± 0.3

high doping concentrations, while the latter leads to decreased mobility at low doping concentrations.[57]

The charge carrier concentrations from capacitive regime measurements and the conductivities from ohmic regime measurements allowed for the calculation of the charge carrier mobility. We further determined the doping efficiency from the charge carrier concentration and the number of dopant molecules per volume. In order to calculate the number of dopant molecules per volume, we first determined the mass densities of each HTL. To this end, we spin coated thin films on 25 mm × 25 mm substrates and subsequently removed the outer 5 mm edge that often contains drying artifacts, obtaining homogeneously coated 15 mm × 15 mm samples. Then, we dissolved the thin film of each sample in 1.8 mL of CB and compared the resulting solutions to reference samples with known concentrations in UV–vis measurements (Figures S13 and S14, Supporting Information). Determination of the layer thickness of equally processed samples by profilometry introduced the largest uncertainty in this procedure. Taking into account the standard deviation of the layer thickness measurements, we obtained densities of 1.29 g cm^{-3} ± 0.03 g cm^{-3} and 1.33 g cm^{-3} ± 0.05 g cm^{-3} for spiro-MeOTAD and **TPCP-3**, respectively. Notably, this is a significant deviation from the density of spiro-MeOTAD that was reported earlier in the literature, i.e., 1.02 g·cm^{-3} ± 0.03 g·cm^{-3} (same method) and 1.82 g cm^{-3} (wafer weight change).[58,59] Details on the measurement precision of our experiment are reported in Figures S13 and S14 (Supporting Information).

Based on the charge carrier densities obtained from MIS-CELIV measurements in the capacitive regime (Figure S15, Supporting Information), we calculated the doping efficiency. However, at an FK209-doping concentration of 3 wt.%, it was impossible to fit the capacitive measurements reliably because the HTLs showed metal-like behavior, approaching the saturation current of the MIS structure. Hence, we could not conclude on charge carrier concentration and mobility in those samples and focused on data from samples with lower FK209-doping concentrations of 0.5 or 1 wt.% in the following. **Table 2** summarizes the electrical properties of FK209-doped thin films of **TPCP-3** and spiro-MeOTAD. The corresponding measurement data and calculations are shown in Figures S11, S12, and S15 (Supporting Information).

The hole density generated in **TPCP-3** was larger than in spiro-MeOTAD at the same doping concentration. This may be a result of higher mass density and doping efficiency. Yet, the standard deviation of the doping efficiency was relatively high because it combined the deviations of both the mass density and the charge carrier concentration. The hole mobility of the FK209-doped samples, which was derived from the hole concentration and the hole conductivity, was about one order of magnitude lower than in neat **TPCP-3** and spiro-MeOTAD, which we attribute to Coulomb trapping of charge carriers.

2.5. Deployment of TPCP-3 in Perovskite Solar Cells

The conductivity of **TPCP-3** thin films that was improved by more than one order of magnitude via doping with FK209 and a favorable IP fulfill the requirements for deployment in solar cells. Hence we incorporated **TPCP-3** as HTL in PSCs utilizing the device architecture indium tin oxide (ITO)/tin oxide (SnO_2)/4-(1′,5′-dihydro-1′-methyl-2′*H*-[5,6]fullereno-C_{60}-I_h-[1,9-c]-pyrrol-2′-yl)benzoic acid (C60-SAM)/$MAPbI_3$/**TPCP-3**/MoO_x/Ag. For reference, we replaced **TPCP-3** with spiro-MeOTAD and investigated the common doping systems LiTFSI:tBP and LiTFSI:tBP:FK209. **Figure 8** shows the *J*–*V* curves of solar cells in the dark and under illumination with both undoped and doped HTLs. In both cases, the undoped references (black curves) exhibit a significant s-shapes, indicating a charge carrier extraction barrier. Since we know from MIS-CELIV measurements that MoO_x forms an ohmic contact to both the silver electrode and the undoped **TPCP-3** or spiro-MeOTAD, we attribute this s-shape to the buildup of space charges due to the low conductivities of the undoped HTLs. These space charges partially screen the electric field across the perovskite and reduce the free energy gradient.[60] As a consequence, part of the electric field drops off across the HTL, effectively shifting the operating point of the perovskite layer toward lower voltages.[61]

To cure the losses in solar cells, enhancing the conductivity of the HTLs by electrical doping is the method of choice. Following the previously discussed strategies, doping of **TPCP-3** with either F_4TCNQ or FK209 produced solar cells without s-shapes (Figure 8a). However, they exhibited roughly 100 mV lower open-circuit voltages (V_{OC}) than solar cells with LiTFSI:tBP-doping or LiTFSI:tBP:FK209-doping. As shown in Figure 8a, doping of **TPCP-3** with the common doping system LiTFSI:tBP did not mitigate the s-shape, even if FK209 was added as a third component. This indicated inefficient doping of the thin film even though FK209 itself can oxidize **TPCP-3** as previously shown in UV-Vis-NIR (Figure 6) and MIS-CELIV measurements (Table 2). The prevailing s-shape in *J*–*V* curves of devices with LiTFSI:tBP:FK209 may have been caused by dedoping, which we also observed for **TPCP-3** doped via FK209 in solution over the course of a few hours when LiTFSI:tBP was present (Figure S16, Supporting Information). Lamberti et al. found dedoping of spiro-MeOTAD by tBP both in the solid state and in solution.[62] They argue that

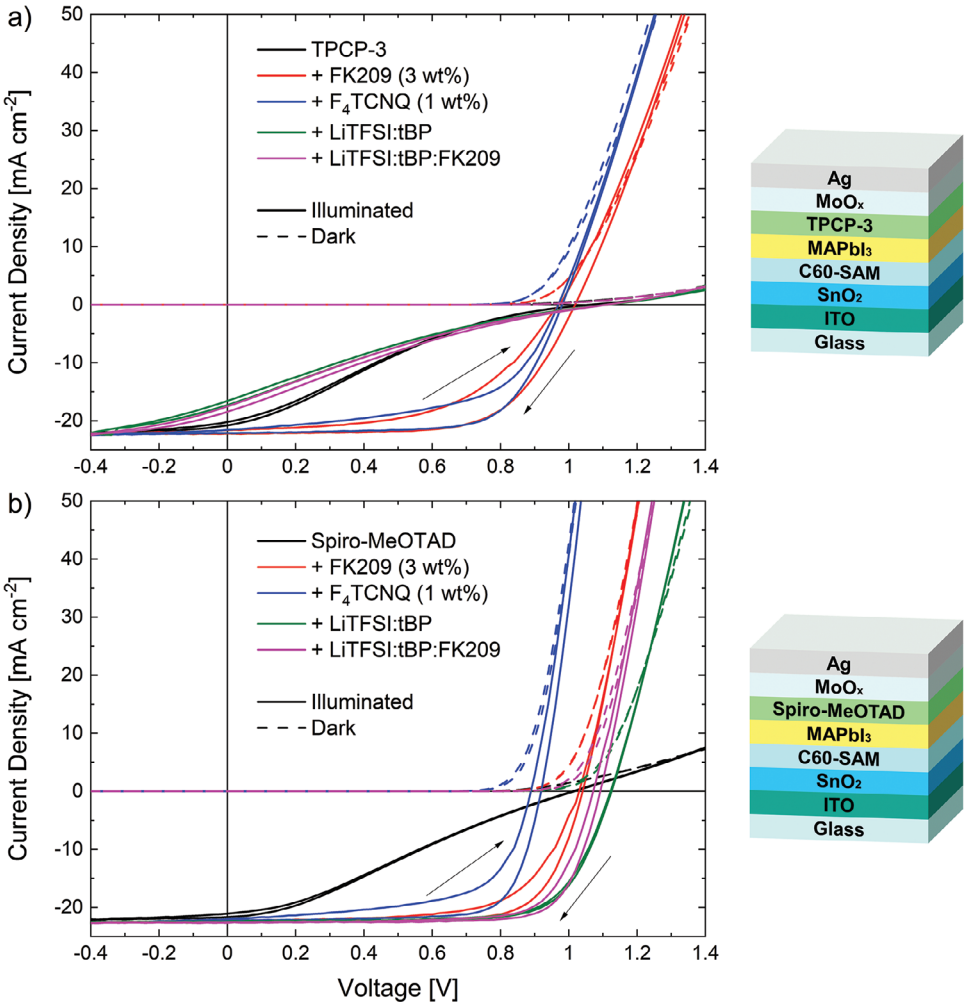

Figure 8. a) *J–V* curves of solar cells comprising HTLs of **TPCP-3**. Devices with undoped **TPCP-3** showed a significant s-shape that was mitigated by FK209-doping and F_4TCNQ-doping, but not by LiTFSI:tBP-doping or LiTFSI:tBP:FK209-doping. b) All doping concepts diminished the s-shape in *J–V* curves of solar cells comprising spiro-MeOTAD.

this is related to charge transfer from spiro-MeOTAD$^+$ species to tBP^0 and subsequent formation of an adduct between the charged tBP$^+$ with another spiro-MeOTAD$^+$ cation ($TFSI^-$ acts as a counter ion). We infer that a similar interaction takes place between **TPCP-3**$^+$ and tBP^0, although at a much higher reaction rate than in spiro-MeOTAD, since we did not observe discoloring of doped spiro-MeOTAD reference solutions even after 21 h (Figure S16, Supporting Information).

The s-shape of *J–V* curves of solar cells comprising spiro-MeOTAD was diminished by all four doping concepts, but again resulted in lower V_{OC}s (Figure 8b). Upon doping of spiro-MeOTAD with F_4TCNQ, the solar cells exhibited V_{OC} = 0.90 V ± 0.02 V, while no doping or FK209-doping resulted in V_{OC}s of 1.01 V ± 0.01 V or 1.03 V ± 0.01 V, respectively. Solar cells comprising spiro-MeOTAD doped with LiTFSI:tBP or LiTFSI:tBP:FK209 exhibited larger V_{OC}s of 1.12 V ± 0.01 V or 1.08 V ± 0.02 V. Summaries of the key parameter statistics are shown in Figures S17–S19 (Supporting Information).

The reduced V_{OC}s may stem from different surface recombination rates at the perovskite/HTL interface.[37,63] Zhang et al. previously found that the concentrations of both the spiro-MeOTAD$^+$ cation and the dopant affect the recombination rate.[64] Furthermore, tBP is known to reduce surface recombination at interfaces.[12] Indeed, in photoluminescence (PL) experiments on spiro-MeOTAD-coated $MAPbI_3$ layers, we observed that neat spiro-MeOTAD quenched the PL of $MAPbI_3$, and only detector noise was visible. In comparison, $MAPbI_3$ coated with spiro-MeOTAD, which included tBP, exhibited a PL intensity enhancement by more than one order of magnitude (Figure S20, Supporting Information). Besides surface passivation, tBP hindering hole extraction may be another origin of the increased PL. In $MAPbI_3$ solar cells, we quantified the impact of tBP on the open-circuit voltage by direct comparison of solar cells with pristine spiro-MeOTAD and solar cells with tBP added to spiro-MeOTAD (Figure S21, Supporting Information). Addition of tBP without any dopants led to an improvement in V_{OC} from 1.01 V ± 0.01 V to 1.11 V ± 0.01 V, i.e., an enhancement of 100 mV. Hence, both doping-induced surface recombination and reduction of surface recombination by tBP are likely causes for the overall loss in V_{OC}.

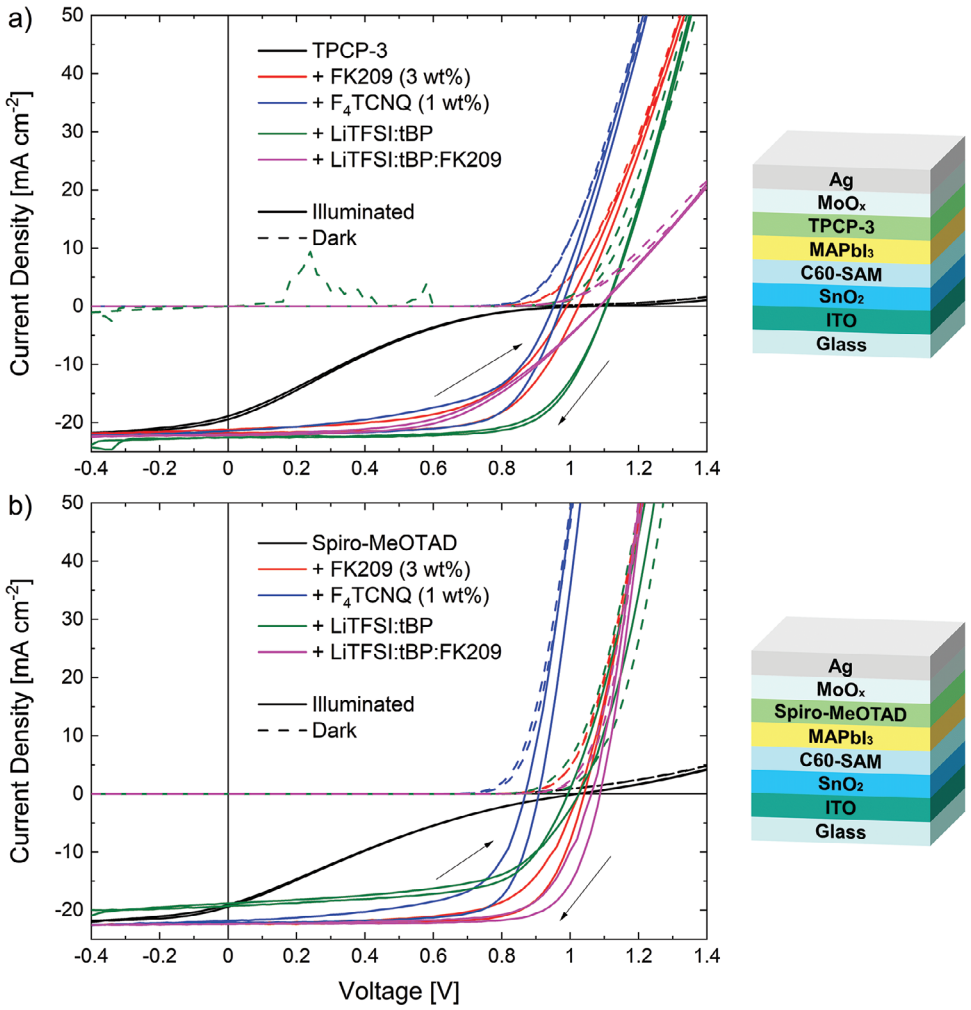

Figure 9. a) *J–V* curves of solar cells comprising **TPCP-3** that were annealed on a hotplate (70 °C, 1 h). Devices with FK209-doped or F_4TCNQ-doped **TPCP-3** maintained their performance. Thermal annealing also cured the s-shape of solar cell with **TPCP-3** layers that were doped with LiTFSI:tBP or LiTFSI:tBP:FK209. b) *J–V* curves of reference solar cells comprising spiro-MeOTAD after annealing. LiTFSI-doping of spiro-MeOTAD led to strongly degrading solar cells, while doping with FK209, F_4TCNQ, or LiTFSI:tBP:FK209 produced more stable devices.

2.6. Thermal Stability of Solar Cells with Doped HTLs

Dopant diffusion can compromise the thermal stability of HTLs. To test for stability, we annealed the devices at temperatures that are well within the expected operation range of solar cells (70 °C, 1 h). Surprisingly, the charge carrier extraction from devices comprising **TPCP-3** doped with LiTFSI:tBP vastly improved through thermal treatment (Figures 8a vs 9a; Figure S17, Supporting Information), enhancing the power conversion efficiency (PCE) from only 3.6% ± 1.1% to 16.7% ± 0.7%. Yet, we observed many electric breakdowns in the dark curves as exemplified in Figure 9a, which we attribute to pinholes in the layer stack. GIWAXS measurements reveal that TPCP-3 forms an amorphous layer (Figure S22, Supporting Information) and its glass transition temperature of 141 °C (Figure S1, Supporting Information) is far above the annealing temperature of 70 °C. Yet, the dopants may aggregate or lead to crystallization of the entire layer by lowering the glass transition temperature.[65] Notably, the glass transition temperature of neat TPCP-3 is 15 °C higher than the glass transition temperature of spiro-MeOTAD, suggesting a better thermal stability.[65]

In contrast, none of the reference devices comprising HTLs doped with LiTFSI:tBP:FK209 showed such an electric breakdown. However, the PCE of these solar cells did only improve from 3.7% ± 0.6% to 11.9% ± 1.4% after annealing whereas LiTFSI:tBP-doped devices reached 16.7% ± 0.7% after annealing. Because of the previously discussed dedoping of tBP, before thermal annealing, **TPCP-3** devices doped with only FK209 (PCE = 13% ± 1.8%) or only F_4TCNQ (PCE = 13.3% ± 1.7%) performed much better than the LiTFSI:tBP:FK209-doped devices. Moreover, they maintained the same performance before and after thermal annealing, demonstrating better thermal stability than devices with any mixture comprising LiTFSI and tBP.

After annealing (70 °C, 1 h), the performance of solar cells comprising spiro-MeOTAD doped with either F_4TCNQ (PCE = 13.8% ± 1.7%) or FK209 (PCE = 16.1% ± 1.2%) remained stable, (Figures 8b vs 9b; Figure S18, Supporting Information). In contrast, solar cells comprising spiro-MeOTAD doped with

Table 3. Comparison of performance parameters of solar cells comprising HTLs from **TPCP-3** or spiro-MeOTAD and employing different doping strategies before and after annealing at 70 °C for 1 h.

		J_{SC} [mA/cm^2]	V_{OC} [V]	FF [%]	PCE [%]
TPCP-3 undoped	Pristine	20.5 ± 0.4	1.06 ± 0.01	21 ± 1	4.5 ± 0.2
	after 70 °C, 1 h	19.0 ± 0.5	1.06 ± 0.01	17 ± 1	3.4 ± 0.2
TPCP-3 + FK209 (3 wt%),	Pristine	21.8 ± 0.4	1.00 ± 0.03	59 ± 6	13.0 ± 1.8
	after 70 °C, 1 h	21.5 ± 0.4	1.00 ± 0.02	62 ± 5	13.3 ± 1.6
TPCP-3 + F_4TCNQ (1 wt%)	Pristine	21.8 ± 0.4	0.97 ± 0.01	63 ± 7	13.3 ± 1.7
	after 70 °C, 1 h	21.6 ± 0.4	0.96 ± 0.02	62 ± 7	12.9 ± 1.8
TPCP-3 + LiTFSI:tBP	Pristine	16.3 ± 3.4	1.11 ± 0.01	20 ± 2	3.6 ± 1.1
	after 70 °C, 1 h	**21.9 ± 0.9**	**1.11 ± 0.01**	**69 ± 3**	**16.7 ± 0.7**
TPCP-3 + LiTFSI:tBP:FK209	Pristine	17.6 ± 2.1	1.10 ± 0.01	19 ± 1	3.7 ± 0.6
	after 70 °C, 1 h	22.2 ± 0.2	1.09 ± 0.01	49 ± 6	11.9 ± 1.4
Spiro-MeOTAD undoped	Pristine	21.4 ± 0.4	1.01 ± 0.01	27 ± 1	5.9 ± 0.2
	after 70 °C, 1 h	18.9 ± 0.7	1.02 ± 0.01	20 ± 1	3.8 ± 0.3
Spiro-MeOTAD + FK209 (3 wt%)	Pristine	22.5 ± 0.4	1.03 ± 0.01	70 ± 4	16.1 ± 1.2
	after 70 °C, 1 h	22.4 ± 0.4	1.03 ± 0.01	70 ± 4	16.0 ± 1.2
Spiro-MeOTAD + F_4TCNQ (1 wt%)	Pristine	22.0 ± 0.3	0.91 ± 0.02	69 ± 7	13.8 ± 1.7
	after 70 °C, 1 h	22.0 ± 0.3	0.89 ± 0.02	68 ± 6	13.3 ± 1.7
Spiro-MeOTAD + LiTFSI:tBP	Pristine	22.1 ± 0.8	1.12 ± 0.01	72 ± 2	17.8 ± 1.0
	after 70 °C, 1 h	19.0 ± 1.1	1.01 ± 0.02	60 ± 3	11.5 ± 1.2
Spiro-MeOTAD + LiTFSI:tBP:FK209	Pristine	22.6 ± 0.2	1.08 ± 0.02	75 ± 2	18.4 ± 0.6
	after 70 °C, 1 h	**22.5 ± 0.2**	**1.07 ± 0.02**	**74 ± 2**	**17.7 ± 0.9**

LiTFSI:tBP degraded from PCE = 17.8% ± 1% to 11.5% ± 1.2%. Remarkably, this PCE deterioration was reduced if FK209 was added to LiTFSI:tBP (LiTFSI:tBP:FK209; before annealing: PCE = 18.4% ± 0.6%; after annealing: PCE = 17.7% ± 0.9%). The comparison of parameters of solar cell comprising HTLs from **TPCP-3** or spiro-MeOTAD before and after annealing is shown in **Table 3**. The combinations performing best after annealing are printed in bold.

HTLs of both **TPCP-3** and spiro-MeOTAD doped with either FK209 or F_4TCNQ yielded solar cells with high thermal stability. FK209 is an efficient standalone dopant for both **TPCP-3** and spiro-MeOTAD, but the lack of surface passivation via tBP limits the V_{OC}.

3. Conclusion

We synthesized three novel HTMs based on TPA units linked to a tetrasubstituted PCP core via thiophene π-bridges. Out of these HTLs, **TPCP-1** with unsubstituted TPA showed a larger hole mobility ($(3.7 \pm 0.3) \cdot 10^{-5}$ cm^2 V^{-1} s^{-1}) than the reference spiro-MeOTAD ($(2.7 \pm 0.3) \cdot 10^{-5}$ cm^2 V^{-1} s^{-1}), but the conductivity of **TPCP-1** was only marginally improved by doping. Yet, the methoxy-substituted derivative **TPCP-3** (IP = 5.27 eV) could be readily doped by FK209 at a doping efficiency similar to spiro-MeOTAD (IP = 5.12 eV). Therefore, **TPCP-3** is a very promising alternative to spiro-MeOTAD, especially in architectures where a larger IP of the HTL is required, e.g. in high-bandgap perovskite solar cells. Moreover, **TPCP-3** is inexpensive compared to spiro-MeOTAD and has a higher glass transition temperature, leveraging better thermal stability. The frequently used dopant system LiTFSI:tBP is problematic for stability and hence, alternative doping strategies should be considered both for spiro-MeOTAD and novel HTLs. FK209 doping increased the conductivity of **TPCP-3** by more than one order of magnitude while showing promising initial device stability. The limited V_{OC} calls for passivation strategies such as functional group engineering of the HTM itself, that render the addition of tBP, which dedopes the HTL, obsolete.

4. Experimental Section

Solar Cell Manufacturing—Substrate Cleaning: Glass substrates (16 × 16 mm^2) with structured indium tin oxide (ITO) electrodes were cleaned in an acetone ultrasonic bath, followed by rubbing with a plastic swab soaked in glass cleaner. Afterwards, the samples were rinsed with isopropanol and dried with a nitrogen gun. Before SnO_2 deposition, the samples were treated in an oxygen plasma for 2 min in order to improve surface wetting.

SnO_2: A SnO_2 colloidal dispersion (Alfa Aesar, 15% weight by weight) was diluted 1:9 with deionized water. The resulting 1.5% weight by weight dispersion was then spin-coated onto the substrates (70 µL, 3000 rpm, 1000 rpm s^{-1}, 30 s), followed by 150 °C thermal annealing in air for 30 min.

C60-SAM: 4-(1′,5′-Dihydro-1′-methyl-2′*H*-[5,6]fullereno-C_{60}-I_h-[1,9-c]-pyrrol-2′-yl)benzoic acid (C60-SAM or C60-COOH-SAM, 99%, Lumtec) was dissolved in tetrahydrofuran (THF, anhydrous, inhibitor-free, 99.9%, Sigma-Aldrich) at 0.5 g L^{-1}, then spin-coated (3000 rpm, 1000 rpm s^{-1}, 30 s) and subsequently thermally annealed (120 °C, 5 min) on a hotplate inside a nitrogen-filled glovebox.

Perovskite: The perovskite precursor solution was prepared by dissolving 1.17 mmol lead iodide (Alfa Aesar ultra dry) and 1.17 mmol methylammonium iodide per mL of 1:1 *N*,*N*-dimethylformamide (DMF, 99.8%, anhydrous, Sigma-Aldrich): *N*-methylpyrrolidone (NMP, 99.5%, extra dry, Acros Organics). After stirring at room temperature for several hours, the solution was filtered with a polytetrafluoroethylene (PTFE) filter (pore size: 0.2 µm). The precursor solution was then spin coated

(3000 rpm, 300 rpm s^{-1}, 30 s) inside a nitrogen filled glovebox and immediately transferred to a heated vacuum chamber (volume: 5 L, temperature: 40 °C), which was evacuated for 60 s using a scroll vacuum pump (12.7 m^3 h^{-1}, nominal final pressure: 0.007 mbar) and then refilled with nitrogen. Furthermore, samples were dried with a nitrogen gun for 60 s, followed by thermal annealing (100 °C, 30 min) on a hotplate inside the glovebox. Subsequently, all sources of solvent vapor were removed from the glovebox.

TPCP-3 and Spiro-MeOTAD. Neat or with FK209 or F_4TCNQ Doping: The hole transport materials were dissolved in chlorobenzene (CB, anhydrous, 99.8%, Sigma-Aldrich) at 30 g L^{-1}. For doping, the indicated amounts of FK209 (Sigma-Aldrich) or F_4TCNQ (OSSILA) were added to the solution. Then they were spin coated (50 µL, 1000 rpm, 1000 rpm s^{-1}, 30 s, drying step 4000 rpm, 10 s) onto the perovskite without any further annealing.

Spiro-MeOTAD with LiTFSI:tBP Doping: Spiro-MeOTAD (99%, Sigma-Aldrich) was dissolved in CB at 50 g L^{-1}. First, 4-*tert*-butylpyridine (tBP, 98%, Sigma-Aldrich) was added and then Lithium bis(trifluoromethanesulfonyl)imide (LiTFSI, 98%, Alfa Aesar) from a 520 g L^{-1} stock solution in acetonitrile (anhydrous, 99.8%, Sigma-Aldrich) to achieve a spiro-MeOTAD:LiTFSI:tBP molar ratio of 1:0.5:2.5. The solution was stored for over 30 min to obtain a homogeneous solution without any precipitate. Afterwards, it was spin coated onto the perovskite (50 µL, 2000 rpm, 1000 rpm s^{-1}, 30 s), followed by 40 h of oxidation in an air-filled dry box with silica gel. The same procedure was conducted in the case of additional 3% by weight (relative to spiro-MeOTAD) FK209 doping.

TPCP-3 with LiTFSI:tBP Doping: TPCP-3 was dissolved in CB at 30 g L^{-1}. LiTFSI and tBP were added at 1:0.5:2.5 molar ratios for a hypothetical 30 g L^{-1} spiro-MeOTAD solution (hence, different molar ratios for TPCP-3). LiTFSI:tBP doped TPCP-3 was then spin coated onto the perovskite layer (1000 rpm, 1000 rpm s^{-1}, 30 s, drying step 4000 rpm, 10 s) and exposed to the same oxidation conditions as LiTFSI:tBP doped spiro-MeOTAD. The same procedure was conducted in the case of additional FK209 doping (LiTFSI:tBP:FK209).

MoO_x/Ag: The top electrode was processed by thermal evaporation in high vacuum through a shadow mask, forming cells with an active area of 10.5 mm^2 each through overlap with the structured ITO bottom electrode. First, molybdenum oxide was evaporated at a rate of ≈1 Å s^{-1} up to a thickness of 10 nm. Next, without breaking vacuum, silver was evaporated on top at a rate of 1 Å s^{-1} up to 10 nm and 2 Å s^{-1} up to the final thickness of 100 nm.

MIS-CELIV Device Manufacturing: The ITO substrates were treated with the same cleaning procedure as for solar cell fabrication. Thereafter, 20 nm of lithium fluoride were thermally evaporated at 1 Å s^{-1} as the insulator. The materials under investigation were dissolved in CB at 30 g L^{-1}. The materials were spin-coated (50 µL, 1000 rpm, 1000 rpm s^{-1}, 30 s), followed by a drying step (4000 rpm, 1000 rpm s^{-1}, 10 s). The process for the MoO_x/Ag top electrode was the same as for the solar cells, except for a smaller active area of 3.5 mm^2 in order to keep the RC constant small.

UV-Vis-NIR Spectroscopy: Absorbance measurements were performed on an Agilent Cary 5000 UV-Vis-NIR spectrometer with a double-beam setup in standard 10.00 mm quartz cuvettes. For the optical energy gap determination, HTM solutions with a concentration of 30 µg mL^{-1} in CB were prepared. Doping of the HTMs was conducted by dissolving F_4TCNQ and FK209 at high concentrations (40 and 200 g L^{-1}) in acetonitrile and then adding these dopant solutions to HTM solutions (10 g L^{-1} in CB). Subsequently, the doped solutions were diluted to an HTM concentration of 30 µg mL^{-1} in CB. A CB reference was measured in the same holder as the solutions and subtracted from the other measurements during data analysis.

Photoelectron Spectroscopy in Air (PESA): Measurements of thin-film ionization potentials (IPs) were carried out on a RIKEN KEIKI AC-2E photoelectron spectrometer. The photoelectron yields were corrected for the quantity of light and fitted with a power number of 0.5 to obtain the IPs.

Solar Cell Characterization: Solar cells were characterized under 1 sun irradiation from a Sciencetech Lightline AX-LA200 solar simulator (AAA, ASTM E927), calibrated with a Newport 91150-KG5 silicon reference solar cell. *J–V* curves were recorded using a source measure unit (Keithley 2420) with sweeps at 300 mV s^{-1} in steps of 20 mV. First, the descending scan from 1.4 to −0.4 V was executed, and then the ascending scan from −0.4 to 1.4 V. After measurements under irradiation (descending – ascending), dark curves were captured (descending – ascending). Measurements were not corrected for spectral mismatch.[66] Spectral mismatch was estimated at 1.02 from other $MAPbI_3$ solar cells measured using the same setup.

MIS-CELIV: A Keysight 81150A function generator was employed to hold a constant injection voltage for a prolonged time, followed by a linear voltage ramp for charge extraction. A slope of 400 mV μs^{-1} was chosen for standard MIS-CELIV measurements of undoped layers and the doping-induced ohmic regime in doped layers. For measurements in the doping-induced capacitive regime, the ramp was lowered to 12 mV μs^{-1}. The resulting transient currents were sent through a transimpedance amplifier Femto DHPCA-100 and captured with a Keysight Infiniium DSO-S104A digital oscilloscope, averaging across 1024 to 4096 measurements for each transient curve. For ohmic regime extraction measurements, a 10 Ω resistor was added in parallel to the transimpedance amplifier input, which reduced the RC constant of the measurement setup to a sixth compared to RC constant with the usual 50 Ω load impedance. The standard deviations of parameters that were obtained from MIS-CELIV measurements were calculated from the standard deviations of the semiconductor layer thicknesses. Further information on how the charge carrier mobilities, doping concentrations and conductivities were calculated can be found in the descriptions of the graphs in the Supporting Information. It was found that it was not feasible to perform reliable transient measurements on samples doped with LiTFSI:tBP, presumably due to mobile Li^+ ions from LiTFSI.

Layer Thicknesses: TPCP and spiro-MeOTAD layer thicknesses were measured with a Dektak XT stylus profilometer on scratched thin films, averaging over several measurements. The standard deviations of the thickness measurements were used to calculate the standard deviations of parameters derived from MIS-CELIV measurements.

Cyclic Voltammetry: Cyclic voltammetry experiments were performed with a Gamry Interface 1010B in a three electrodes electrochemical cell. The electrochemical cell was equipped with a glassy carbon (GC) working electrode, $Ag/AgNO_3$ reference electrode, and a platinum counter electrode.

The experiments were performed in N_2-saturated *N,N*-dimethylformamide containing 0.1 M [nBu$_4$N][PF_6] as the electrolyte at a scan rate of 100 mV s^{-1}. The concentration of the investigated compounds was 3 mM. According to the IUPAC recommendation, ferrocene (Fc) was added as an internal standard after each experiment.[39]

Synthesis: Details of synthetic procedures and further characterization of the compounds can be found in the Supporting Information.

Density Functional Theory Calculations: The TPCP conformers for the theoretical calculations were generated using the previously reported workflow.[6] The CREST sampling was omitted. 2000 (4000 for TPCP-1) initial conformers were generated with the ETKDG (experimental-torsion distance geometry with basic knowledge) method and filtered using a root-mean-square deviation (RMSD) threshold of 2 Å (1 Å for TPCP-1) in the first step and of 1 Å in the second step.[67] Afterward, at most 10 of the remaining conformers (5 for TPCP-1, 8 for TPCP-2, and 10 for TPCP-3) were used for the DFT and TD-DFT calculations, which were performed using TURBOMOLE, version 7.4.1.[68] The conformers were optimized with the def2-SVP basis set,[69] and all calculations were run with the B3LYP functional,[70–73] using the Grimme DFT-D3 dispersion correction with Becke-Johnson damping.[74,75] The multipole accelerated Resolution of Identity approximation for the Coulomb term was applied for all calculations.[76–82] In all cases, restricted calculations were performed for the closed-shell neutral TPCP molecules and unrestricted calculations for the TPCP cations. Starting with the optimized geometries of the lowest-energy conformer of neutral TPCPs, the respective cations were also optimized. Using the optimized structure of neutral and oxidized TPCPs, single-point calculations were performed using B3LYP/def2-TZVP,[83] from which the IPs and orbital energies were obtained. The IP was calculated as the difference between the total DFT energy for charged molecule (+1) and the total energy for the neutral molecule. Ten singlet-singlet

vertical excitations for the neutral molecules and forty vertical excitations for the cations were performed with TD-DFT using B3LYP/def2-SVP in the gas phase.[84–89] As a comparison, the excitations of the neutral TPCPs were also calculated with the def2-TZVP basis set and are shown in Figure S23 (Supporting Information). A consistent small blue-shift of 11–12 nm (0.056–0.061 eV) for the results obtained with the def2-SVP basis set was observed. Spectra were generated using Gaussian broadening with a full width at half maximum (FWHM) of 0.1 eV. An isovalue of 0.0005 a.u. was used for the visualization of electron density differences.

Supporting Information

Supporting Information is available from the Wiley Online Library or from the author.

Acknowledgements

The authors thank C. Zippel and P. Turpel for their help in conducting synthesis of the precursors. All authors acknowledge funding by the Carl Zeiss Foundation (project KeraSolar). H.R. and A.C. acknowledge further support by the Helmholtz Association (program Materials and Technologies for the Energy Transition, MTET). M.K and S.B. acknowledge Deutsche Forschungsgemeinschaft under Germany's Excellence Strategy for the Excellence Cluster "3D Matter Made to Order" (Grant No. EXC-2082/1–390761711). The computational work was performed on the HoreKa supercomputer funded by the Ministry of Science, Research and the Arts Baden-Württemberg and by the Federal Ministry of Education and Research. [Correction added on May 30, 2024, after first online publication: Table 3 has been corrected.]

Open access funding enabled and organized by Projekt DEAL.

Conflict of Interest

The authors declare no conflict of interest.

Data Availability Statement

The data that support the findings of this study are available from the corresponding author upon reasonable request.

Keywords

density functional theory, electrical doping, hole mobilities, hole transport layers, MIS-CELIV, paracyclophanes, perovskite solar cells

Received: February 2, 2024
Revised: May 15, 2024
Published online:

[1] E. Unger, T. J. Jacobsson, *ACS Energy Lett.* **2022**, *7*, 1240.
[2] H. S. Kim, C. R. Lee, J. H. Im, K. B. Lee, T. Moehl, A. Marchioro, S. J. Moon, R. Humphry-Baker, J. H. Yum, J. E. Moser, M. Grätzel, N. G. Park, *Sci. Rep.* **2012**, *2*, 591.
[3] S. Park, J. H. Heo, C. H. Cheon, H. Kim, S. H. Im, H. J. Son, *J. Mater. Chem. A* **2015**, *3*, 24215.
[4] S. Park, J. H. Heo, J. H. Yun, T. S. Jung, K. Kwak, M. J. Ko, C. H. Cheon, J. Y. Kim, S. H. Im, H. J. Son, *Chem. Sci.* **2016**, *7*, 5517.
[5] Y. S. Lin, H. Li, W. S. Yu, S. T. Wang, Y. M. Chang, T. H. Liu, S. S. Li, M. Watanabe, H. H. Chiu, D. Y. Wang, Y. J. Chang, *J. Power Sources* **2021**, *491*, 229543.
[6] S. A. Otterbach, D. Elsing, A. D. Schulz, H. Tappert, W. Wenzel, M. Kozlowska, H. Röhm, S. Bräse, *Adv. Funct. Mater.* **2023**, 2309226.
[7] A. Abate, T. Leijtens, S. Pathak, J. Teuscher, R. Avolio, M. E. Errico, J. Kirkpatrik, J. M. Ball, P. Docampo, I. McPherson, H. J. Snaith, *Phys. Chem. Chem. Phys.* **2013**, *15*, 2572.
[8] L. K. Ono, P. Schulz, J. J. Endres, G. O. Nikiforov, Y. Kato, A. Kahn, Y. Qi, *J. Phys. Chem. Lett.* **2014**, *5*, 1374.
[9] C. Ding, R. Huang, C. Ahläng, J. Lin, L. Zhang, D. Zhang, Q. Luo, F. Li, R. Österbacka, C. Q. Ma, *J. Mater. Chem. A* **2021**, *9*, 7575.
[10] H. Djellab, M. Armand, D. Delabouglise, *Synth. Met.* **1995**, *74*, 223.
[11] S. Wang, M. Sina, P. Parikh, T. Uekert, B. Shahbazian, A. Devaraj, Y. S. Meng, *Nano Lett.* **2016**, *16*, 5594.
[12] M. Dürr, A. Yasuda, G. Nelles, *Appl. Phys. Lett.* **2006**, *89*, 061110.
[13] L. Calio, S. Kazim, M. Grätzel, S. Ahmad, *Angew. Chem., Int. Ed.* **2016**, *55*, 14522.
[14] Z. H. Bakr, Q. Wali, A. Fakharuddin, L. Schmidt-Mende, T. M. Brown, R. Jose, *Nano Energy* **2017**, *34*, 271.
[15] M. Urbani, G. de la Torre, M. K. Nazeeruddin, T. Torres, *Chem. Soc. Rev.* **2019**, *48*, 2738.
[16] D. Molina, J. Follana-Berná, Á. Sastre-Santos, *J. Mater. Chem. C* **2023**, *11*, 7885.
[17] W. Li, H. Dong, L. Wang, N. Li, X. Guo, J. Li, Y. Qiu, *J. Mater. Chem. A* **2014**, *2*, 13587.
[18] Y. Yue, N. T. Salim, Y. Wu, X. Yang, A. Islam, W. Chen, J. Liu, E. Bi, F. Xie, M. Cai, L. Han, *Adv. Mater.* **2016**, *28*, 10738.
[19] G. Ren, W. Han, Q. Zhang, Z. Li, Y. Deng, C. Liu, W. Guo, *Nano-Micro Lett.* **2022**, *14*, 175.
[20] B. Xu, Z. Zhu, J. Zhang, H. Liu, C. C. Chueh, X. Li, A. K. Y. Jen, *Adv. Energy Mater.* **2017**, *7*, 1700683.
[21] J. Burschka, F. Kessler, M. K. Nazeeruddin, M. Grätzel, *Chem. Mater.* **2013**, *25*, 2986.
[22] J. Luo, C. Jia, Z. Wan, F. Han, B. Zhao, R. Wang, *J. Power Sources* **2017**, *342*, 886.
[23] M. Liu, S. Dahlström, C. Ahläng, S. Wilken, A. Degterev, A. Matuhina, M. Hadadian, M. Markkanen, K. Aitola, A. Kamppinen, J. Deska, O. Mangs, M. Nyman, P. D. Lund, J. H. Smått, R. Österbacka, P. Vivo, *J. Mater. Chem. A* **2022**, *10*, 11721.
[24] Y. Dienes, S. Durben, T. Kárpáti, T. Neumann, U. Englert, L. Nyulászi, T. Baumgartner, *Chem. - Eur. J.* **2007**, *13*, 7487.
[25] D. Lumpi, B. Holzer, J. Bintinger, E. Horkel, S. Waid, H. D. Wanzenböck, M. Marchetti-Deschmann, C. Hametner, E. Bertagnolli, I. Kymissis, J. Fröhlich, *New J. Chem.* **2015**, *39*, 1840.
[26] T. Y. Li, C. Su, S. B. Akula, W. G. Sun, H. M. Chien, W. R. Li, *Org. Lett.* **2016**, *18*, 3386.
[27] K. Kobayakawa, M. Hasegawa, H. Sasaki, J. Endo, H. Matsuzawa, K. Sako, J. Yoshida, Y. Mazaki, *Chem. Asian J.* **2014**, *9*, 2751.
[28] E. H. Jung, N. J. Jeon, E. Y. Park, C. S. Moon, T. J. Shin, T. Y. Yang, J. H. Noh, J. Seo, *Nature* **2019**, *567*, 511.
[29] H. Kirihata, M. Uda, *Rev. Sci. Instrum.* **1981**, *52*, 68.
[30] M. Uda, *Jpn. J. Appl. Phys.* **1985**, *24*, 284.
[31] M. Uda, Y. Nakagawa, T. Yamamoto, M. Kawasaki, A. Nakamura, T. Saito, K. Hirose, *J. Electron Spectrosc. Relat. Phenom.* **1998**, *88–91*, 767.
[32] A. Amirav, U. Even, J. Jortner, *J. Chem. Phys.* **1981**, *75*, 2489.
[33] H. Yoshida, K. Yamada, J. Tsutsumi, N. Sato, *Phys. Rev. B* **2015**, *92*, 075145.
[34] S. Olthof, *APL Mater.* **2016**, *4*, 091502.
[35] S. M. Park, S. M. Mazza, Z. Liang, A. Abtahi, A. M. Boehm, S. R. Parkin, J. E. Anthony, K. R. Graham, *ACS Appl. Mater. Interfaces* **2018**, *10*, 15548.
[36] T. J. Jacobsson, J. P. Correa-Baena, M. Pazoki, M. Saliba, K. Schenk, M. Grätzel, A. Hagfeldt, *Energy Environ. Sci.* **2016**, *9*, 1706.
[37] M. Stolterfoht, P. Caprioglio, C. M. Wolff, J. A. Márquez, J. Nordmann, S. Zhang, D. Rothhardt, U. Hörmann, Y. Amir, A. Redinger, L.

Kegelmann, F. Zu, S. Albrecht, N. Koch, T. Kirchartz, M. Saliba, T. Unold, D. Neher, *Energy Environ. Sci.* **2019**, *12*, 2778.
[38] S. Fantacci, F. De Angelis, M. K. Nazeeruddin, M. Grätzel, *J. Phys. Chem. C* **2011**, *115*, 23126.
[39] R. R. Gagné, C. A. Koval, G. C. Lisensky, *Inorg. Chem.* **1980**, *19*, 2854.
[40] G. Juška, N. Nekrašas, K. Genevičius, *J. Non-Cryst. Solids* **2012**, *358*, 748.
[41] O. J. Sandberg, M. Nyman, S. Dahlström, S. Sandén, B. Törngren, J. H. Smått, R. Österbacka, *Appl. Phys. Lett.* **2017**, *110*, 153504.
[42] Z. Ma, Z. Xiao, Q. Liu, D. Huang, W. Zhou, H. Jiang, Z. Yang, M. Zhang, W. Zhang, Y. Huang, *ACS Appl. Mater. Interfaces* **2020**, *12*, 52779.
[43] W. Gao, A. Kahn, *Appl. Phys. Lett.* **2001**, *79*, 4040.
[44] K. Kanai, K. Akaike, K. Koyasu, K. Sakai, T. Nishi, Y. Kamizuru, T. Nishi, Y. Ouchi, K. Seki, *Appl. Phys. A* **2009**, *95*, 309.
[45] Z. Q. Gao, B. X. Mi, G. Z. Xu, Y. Q. Wan, M. L. Gong, K. W. Cheah, C. H. Chen, *Chem. Commun.* **2008**, *1*, 117.
[46] J. Li, G. Zhang, D. M. Holm, I. E. Jacobs, B. Yin, P. Stroeve, M. Mascal, A. J. Moulé, *Chem. Mater.* **2015**, *27*, 5765.
[47] J. Li, I. Duchemin, O. M. Roscioni, P. Friederich, M. Anderson, E. D. Como, G. Kociok-Köhn, W. Wenzel, C. Zannoni, D. Beljonne, X. Blase, G. D'Avino, *Mater. Horiz.* **2019**, *6*, 107.
[48] A. Fediai, F. Symalla, P. Friederich, W. Wenzel, *Nat. Commun.* **2019**, *10*, 4547.
[49] U. B. Cappel, T. Daeneke, U. Bach, *Nano Lett.* **2012**, *12*, 4925.
[50] S. Panja, U. Kadhane, J. U. Andersen, A. I. S. Holm, P. Hvelplund, M. B. Suhr Kirketerp, S. Brøndsted Nielsen, K. Støchkel, R. N. Compton, J. S. Forster, K. Kilså, M. Brøndsted Nielsen, *J. Chem. Phys.* **2007**, *127*, 124301.
[51] G. Juška, K. Arlauskas, M. Viliūnas, J. Kočka, *Phys. Rev. Lett.* **2000**, *84*, 4946.
[52] O. J. Sandberg, M. Nyman, R. Österbacka, *Org. Electron.* **2014**, *15*, 3413.
[53] M. Nyman, O. J. Sandberg, W. Li, S. Zeiske, R. Kerremans, P. Meredith, A. Armin, *Sol. RRL* **2021**, *5*, 2100018.
[54] V. I. Arkhipov, P. Heremans, E. V. Emelianova, G. J. Adriaenssens, H. Bässler, *Appl. Phys. Lett.* **2003**, *82*, 3245.
[55] C. Tanase, E. J. Meijer, P. W. M. Blom, D. M. de Leeuw, *Phys. Rev. Lett.* **2003**, *91*, 216601.
[56] S. D. Baranovskii, *Phys. Status Solidi B* **2014**, *251*, 487.
[57] V. I. Arkhipov, E. V. Emelianova, P. Heremans, H. Bässler, *Phys. Rev. B* **2005**, *72*, 235202.
[58] P. Docampo, A. Hey, S. Guldin, R. Gunning, U. Steiner, H. J. Snaith, *Adv. Funct. Mater.* **2012**, *22*, 5010.
[59] I.-K. Ding, N. Tétreault, J. Brillet, B. E. Hardin, E. H. Smith, S. J. Rosenthal, F. Sauvage, M. Grätzel, M. D. McGehee, *Adv. Funct. Mater.* **2009**, *19*, 2431.
[60] U. Würfel, A. Cuevas, P. Würfel, *IEEE J. Photovoltaics* **2015**, *5*, 461.
[61] W. Tress, *Organic Solar Cells*, Springer Series in Materials Science, Vol. *208*, Springer, Cham **2014**.
[62] F. Lamberti, T. Gatti, E. Cescon, R. Sorrentino, A. Rizzo, E. Menna, G. Meneghesso, M. Meneghetti, A. Petrozza, L. Franco, *Chem* **2019**, *5*, 1806.
[63] S. Yang, J. Dai, Z. Yu, Y. Shao, Y. Zhou, X. Xiao, X. C. Zeng, J. Huang, *J. Am. Chem. Soc.* **2019**, *141*, 5781.
[64] J. Zhang, Q. Daniel, T. Zhang, X. Wen, B. Xu, L. Sun, U. Bach, Y. B. Cheng, *ACS Nano* **2018**, *12*, 10452.
[65] E. Kasparavicius, A. Magodemov, T. Malinauskas, V. Getautis, *Chem. - Eur. J.* **2018**, *24*, 9910.
[66] C. H. Seaman, *Sol. Energy* **1982**, *29*, 291.
[67] S. Riniker, G. A. Landrum, *J. Chem. Inf. Model.* **2015**, *55*, 2562.
[68] S. G. Balasubramani, G. P. Chen, S. Coriani, M. Diedenhofen, M. S. Frank, Y. J. Franzke, F. Furche, R. Grotjahn, M. E. Harding, C. Hättig, A. Hellweg, B. Helmich-Paris, C. Holzer, U. Huniar, M. Kaupp, A. M. Khah, S. K. Khani, T. Müller, F. Mack, B. D. Nguyen, S. M. Parker, E. Perlt, D. Rappoport, K. Reiter, S. Roy, M. Rückert, G. Schmitz, M. Sierka, E. Tapavicza, D. P. Tew, et al., *J. Chem. Phys.* **2020**, *152*, 184107.
[69] A. Schäfer, H. Horn, R. Ahlrichs, *J. Chem. Phys.* **1992**, *97*, 2571.
[70] S. H. Vosko, L. Wilk, M. Nusair, *Can. J. Phys.* **1980**, *58*, 1200.
[71] C. Lee, W. Yang, R. G. Parr, *Phys. Rev. B* **1988**, *37*, 785.
[72] P. J. Stephens, F. J. Devlin, C. F. Chabalowski, M. J. Frisch, *J. Phys. Chem.* **1994**, *98*, 11623.
[73] S. Grimme, *J. Comput. Chem.* **2006**, *27*, 1787.
[74] S. Grimme, J. Antony, S. Ehrlich, H. Krieg, *J. Chem. Phys.* **2010**, *132*, 154104.
[75] S. Grimme, S. Ehrlich, L. Goerigk, *J. Comput. Chem.* **2011**, *32*, 1456.
[76] O. Treutler, R. Ahlrichs, *J. Chem. Phys.* **1995**, *102*, 346.
[77] K. Eichkorn, O. Treutler, H. Öhm, M. Häser, R. Ahlrichs, *Chem. Phys. Lett.* **1995**, *242*, 652.
[78] K. Eichkorn, F. Weigend, O. Treutler, R. Ahlrichs, *Theor. Chem. Acc.* **1997**, *97*, 119.
[79] M. Von Arnim, R. Ahlrichs, *J. Comput. Chem.* **1999**, *19*, 1746.
[80] F. Weigend, *Phys. Chem. Chem. Phys.* **2002**, *4*, 4285.
[81] M. Sierka, A. Hogekamp, R. Ahlrichs, *J. Chem. Phys.* **2003**, *118*, 9136.
[82] F. Weigend, *Phys. Chem. Chem. Phys.* **2006**, *8*, 1057.
[83] A. Schäfer, C. Huber, R. Ahlrichs, *J. Chem. Phys.* **1994**, *100*, 5829.
[84] R. Bauernschmitt, R. Ahlrichs, *Chem. Phys. Lett.* **1996**, *256*, 454.
[85] R. Bauernschmitt, M. Häser, O. Treutler, R. Ahlrichs, *Chem. Phys. Lett.* **1997**, *264*, 573.
[86] S. Grimme, F. Furche, R. Ahlrichs, *Chem. Phys. Lett.* **2002**, *361*, 321.
[87] F. Furche, R. Ahlrichs, *J. Chem. Phys.* **2002**, *117*, 7433.
[88] F. Furche, D. Rappoport, *J. Theor. Comput. Chem.* **2005**, *16*, 93.
[89] D. Rappoport, F. Furche, *J. Chem. Phys.* **2005**, *122*, 064105.